HHS Public Access

Author manuscript

Phys Med Biol. Author manuscript; available in PMC 2016 August 21.

Published in final edited form as:

Phys Med Biol. 2015 August 21; 60(16): 6563–6583. doi:10.1088/0031-9155/60/16/6563.

Transmission-less attenuation estimation from time-of-flight PET histo-images using consistency equations

Yusheng Li[1], **Michel Defrise**[2], **Scott D Metzler**[1], and **Samuel Matej**[1]

Yusheng Li: yushli@mail.med.upenn.edu

[1]Department of Radiology, University of Pennsylvania, Philadelphia, PA 19104 USA

[2]Department of Nuclear Medicine, Vrije Universiteit Brussel, B-1090, Brussels, Belgium

Abstract

In positron emission tomography (PET) imaging, attenuation correction with accurate attenuation estimation is crucial for quantitative patient studies. Recent research showed that the attenuation sinogram can be determined up to a scaling constant utilizing the time-of-flight information. The TOF-PET data can be naturally and efficiently stored in a histo-image without information loss, and the radioactive tracer distribution can be efficiently reconstructed using the DIRECT approaches. In this paper, we explore transmission-less attenuation estimation from TOF-PET histo-images. We first present the TOF-PET histo-image formation and the consistency equations in the histo-image parameterization, then we derive a least-squares solution for estimating the directional derivatives of the attenuation factors from the measured emission histo-images. Finally, we present a fast solver to estimate the attenuation factors from their directional derivatives using the discrete sine transform and fast Fourier transform while considering the boundary conditions. We find that the attenuation histo-images can be uniquely determined from the TOF-PET histo-images by considering boundary conditions. Since the estimate of the attenuation directional derivatives can be inaccurate for LORs tangent to the patient boundary, external sources, e.g., a ring or annulus source, might be needed to give an accurate estimate of the attenuation gradient for such LORs. The attenuation estimation from TOF-PET emission histo-images is demonstrated using simulated 2D TOF-PET data.

Keywords

Attenuation estimation; histo-image; consistency equations; John's equation; time-of-flight (TOF); positron emission tomography (PET)

1. Introduction

In positron emission tomography (PET) imaging, attenuation correction with accurate attenuation estimation is crucial for quantitative patient studies. For a modern PET scanner combined with an x-ray computed tomography (CT) scanner, the attenuation image is usually estimated from the x-ray CT scan, scaled to the PET energy of 511 keV, and forward projected to obtain the attenuation sinogram (Kinahan et al. 1998). However there are situations where the CT-based attenuation is incomplete or inaccurate, due to, e.g., the mismatch between PET and CT scans because of patient motion or different respiratory pattern during and between the two scans. PET images reconstructed without attenuation

correction, or with an incomplete or mis-registered attenuation image can produce severe attenuation artifacts and lead to diagnostic errors (Gould et al. 2007). The newly emerged PET/MR scanners allow simultaneous data acquisitions of both PET functional imaging and high resolution MR anatomical imaging. However, the relation between the MR measurements and the linear attenuation coefficient at 511 keV is complex. Despite limited success in segmenting the registered MR images with attenuation assignment (Martinez-Möller et al. 2009, Hofmann et al. 2011, Keereman et al. 2013, Burgos et al. 2014), attenuation correction for PET/MR scanners remains more prone to errors than for PET-CT scanners (Wagenknecht et al. 2013).

TOF-PET data contain substantially more information about attenuation than non-TOF-PET data. Defrise et al. (2012) showed that TOF-PET data can determine the attenuation sinogram up to a constant, which results in a multiplicative factor in the activity image. Maximum likelihood methods were also developed to allow simultaneous reconstructions of attenuation and activity for TOF PET (Rezaei et al. 2012, Defrise et al. 2014, Rezaei et al. 2014).

An efficient partitioning scheme for TOF-PET data is the view-grouped histo-images (Matej et al. 2009, Daube-Witherspoon et al. 2012). The histo-images can be obtained by depositing TOF-PET events into the image space at the most likely annihilation (MLA) position or the confidence-weighted (CW) positions (Snyder et al. 1981, Watson 2007, Matej et al. 2009). The goal of this paper is to explore transmissionless attenuation estimation from the consistent TOF-PET histo-images. We first present the TOF-PET histo-image formation and the consistency equations in the histo-image parameterization. We then derive a least-squares (LS) solution for estimating the directional derivatives of the attenuation factors, which was parameterized in the histo-images format. Finally, we present a fast solver to estimate the attenuation factors from their directional derivatives using the discrete sine transform and fast Fourier transform.

2. Attenuation estimation from histo-image

2.1. TOF-PET histo-image formulation

TOF-PET data are generally parameterized as

$$p(t,s,\phi,z,\theta)=\int_{-\infty}^{\infty}\mathrm{d}l\,h_F(t-l)\times f(s\cos\phi-l\cos\theta\sin\phi,\ s\sin\phi+l\cos\theta\cos\phi,\ z+l\sin\theta), \quad (1)$$

where f is a 3D tracer distribution and the $h_F(t-l)$ is a TOF profile centered at position $l=t$ along the line-of-response (LOR), t is the TOF parameter, s and φ are the usual sinogram coordinates, z is the axial coordinate of the midpoint of the LOR, and θ is the co-polar angle between the LOR and a transaxial plane. The TOF profile is modeled as a Gaussian distribution with standard deviation σ_F,

$$h_F(t)=\frac{1}{\sqrt{2\pi}\sigma_F}\exp\left(-\frac{t^2}{2\sigma_F^2}\right). \quad (2)$$

The TOF parameter t is related with the TOF time difference ΔT between the two arrival times of the two gammas by $t = c\Delta T/2$ where c denotes the speed of light. The standard deviation $\sigma_F = cT_{\mathrm{FWHM}}/(4\sqrt{2\log 2})$, and T_{FWHM} is the full width at half maximum (FWHM) of the measured time difference, which is on the order of 500 ps in current clinical scanners (Karp et al. 2008, Surti et al. 2007, Zaidi et al. 2011). A $LaBr_3$-based PET scanner developed at Penn has a timing resolution of 375 ps (Daube-Witherspoon et al. 2010), and a newly emerged scanner, Philips Vereos PET/CT based on digital photon counting technology, has a timing resolution of 345 ps.

The histo-image can be obtained by first grouping the TOF-PET events by the TOF direction n depending on the azimuthal angle φ and co-polar angle θ. Then each event is deposited/backprojected into the image space at the most likely annihilation (MLA) position or the confidence-weighted (CW) positions (Snyder et al. 1981, Watson 2007, Matej et al. 2009). As shown in figure 1, each measured event associated with a single positron annihilation can be determined by the two detectors A and B and the difference of arrival time t of the gammas at the two locations. The MLA position x and the direction n of a TOF event are

$$\begin{aligned}\vec{x} &= (s\cos\phi - t\cos\theta\sin\phi,\ s\sin\phi + t\cos\theta\cos\phi,\ z + t\sin\theta)^T \\ \hat{n} &= (-\cos\theta\sin\phi,\ \cos\theta\cos\phi,\ \sin\theta)^T,\end{aligned} \quad (3)$$

where T denotes the vector or matrix transpose. We can use the MLA position $x \in \mathbb{R}^3$ and the direction $n \in S^2$ to parameterize and formulate the histo-image. An individual measured event determines a point $(x, \vec{n})$ in a 5D measurement space $\mathcal{M} = \mathbb{R}^3 \times S^2$, where $\mathbb{R}^3$ and S^2 denote the 3D Euclidean space and the unit sphere in 3D space. The measurements obtained over an entire PET experiment form a Poisson point process on $\mathcal{M}$ (Snyder et al. 1981, Snyder and Miller 1991). The expectation histo-image $q(x, \vec{n})$ can be modeled as a convolution

$$q(\vec{x}, \hat{n}) = \int_{-\infty}^{\infty} \mathrm{d}l\, h_B(t-l)\, p(l, s, \phi, z, \theta), \quad (4)$$

where $h_B(t)$ is the backprojection TOF profile and it can also be selected as a Gaussian distribution with standard deviation σ_B. One can use $h_B(t) = \delta(t)$ with $\sigma_B = 0$ and $h_B(t) = h_F(t)$ with $\sigma_B = \sigma_F$ for MLA and CW depositions, respectively.

Putting (1) into (4), we obtain

$$q(\vec{x}, \hat{n}) = \int_{-\infty}^{\infty} \mathrm{d}l\, h(l)\, f(\vec{x} - l\hat{n}), \quad (5)$$

where $h(t)$ is defined by the convolution of $h_B(t)$ and $h_F(t)$ as

$$h(t) = h_B * h_F(t) = \frac{1}{\sqrt{2\pi}\sigma}\exp\left(-\frac{t^2}{2\sigma^2}\right), \sigma = \sqrt{\sigma_B^2 + \sigma_F^2}. \quad (6)$$

Equation (5) is the histo-image formulation with parameters x and n. The standard deviation σ in the CW histo-image is increased by a factor of $\sqrt{2}$ compared to that in the MLA histo-image.

Some of the derivations below use two unit vectors $\hat{u}$ and v that are orthogonal to n. All results in the paper are valid independently of the choice of these vectors. Some results will be made explicit, using the usual convention, which corresponds to the sinogram parameterization in (1). The two auxiliary unit vectors $\hat{u}$, v are given by

$$\hat{u}=(\cos\phi,\sin\phi,0)^T, \quad (7)$$

$$\hat{v}=\hat{n}\times\hat{u}=(-\sin\theta\sin\phi,\sin\theta\cos\phi,-\cos\theta)^T. \quad (8)$$

Using these vectors, we can rewrite (5) as a 3D convolution

$$q(\vec{x},\hat{n})=f(\vec{x})***\kappa(\vec{x},\hat{n}),\qquad \kappa(\vec{x},\hat{n})=h(\vec{x}\cdot\hat{n})\,\delta(\vec{x}\cdot\hat{u})\,\delta(\vec{x}\cdot\hat{v}). \quad (9)$$

Equation (9) states that the expectation $q(x,\vec{n})$ is a 3D convolution of the activity distribution $f(x)$ and the TOF kernel $\kappa(x,\vec{n})$.

2.2. Histo-image consistency equations

The histo-image $q(x,\vec{n})$ has five degrees of freedom (depends on five parameters) and the object $f(x)$ has only three—the two degrees of redundancy can be expressed as two independent consistency equations (Defrise et al. 2008, Defrise et al. 2013). For TOF-PET histo-images expressed in (4), (5) or (9), the vector calculus form of the consistency equations is (Defrise et al. 2015, Li et al. 2015)

$$\diamond q(\vec{x},\hat{n})=\nabla_{\hat{n}}q(\vec{x},\hat{n})-\sigma^2\hat{n}\cdot\nabla\nabla q(\vec{x},\hat{n})=0. \quad (10)$$

Here we define $\diamond=\nabla_n-\sigma^2 n\cdot\nabla\nabla$ which maps $q(x,\vec{n})$ onto a vector field, the k-th component $\diamond_k=\frac{\partial}{\partial\hat{n}_k}-\sigma^2\sum_{i=1}^{3}\hat{n}_i\frac{\partial^2}{\partial x_i\partial x_k}$, k = 1, 2, 3, ∇ is the gradient with respect to position x and ∇_n is the gradient with respect to TOF direction n. An alternative proof of (10) is given in Appendix A. Since the TOF direction n is normalized, i.e., $\|n\|$ = 1, ∇_n is only meaningful in the directions perpendicular to n, e.g, $\hat{u}$ and v. All directions perpendicular to n can be represented as a combination of $\hat{u}$ and v, so it is sufficient to consider the following two basis consistency equations

$$\hat{u}\cdot\nabla_{\hat{n}}q(\vec{x},\hat{n})-\sigma^2(\hat{n}\cdot\nabla)(\hat{u}\cdot\nabla)q(\vec{x},\hat{n})=0. \quad (11)$$

$$\hat{v}\cdot\nabla_{\hat{n}}q(\vec{x},\hat{n})-\sigma^2(\hat{n}\cdot\nabla)(\hat{v}\cdot\nabla)q(\vec{x},\hat{n})=0. \quad (12)$$

The consistency equations (10), (11) and (12) are independent of the coordinate system. For the specific parameterization (7) and (8), one has the following link with angular derivatives:

$$\hat{u}\cdot\nabla_{\hat{n}}=-\frac{1}{\cos\theta}\frac{\partial\hat{n}}{\partial\phi}\cdot\nabla_{\hat{n}}=-\sec\theta\frac{d}{d\phi}, \quad (13)$$

$$\hat{v}\cdot\nabla_{\hat{n}}=-\frac{\partial\hat{n}}{\partial\theta}\cdot\nabla_{\hat{n}}=-\frac{d}{d\theta}. \quad (14)$$

Here, we used $\frac{\partial\hat{n}}{\partial\phi}=-\cos\theta\hat{u}$ and $\frac{\partial\hat{n}}{\partial\theta}=-\hat{v}$. Another useful consistency equation can be derived by adding $v\hat{\cdot}\nabla$ (11) and $-\hat{u}\cdot\nabla$ (12):

$$(\hat{v}\cdot\nabla)(\hat{u}\cdot\nabla_{\hat{n}})q(\vec{x},\hat{n})-(\hat{u}\cdot\nabla)(\hat{v}\cdot\nabla_{\hat{n}})q(\vec{x},\hat{n})=0. \quad (15)$$

Equation (15) is John's equation for TOF-PET histo-images (John 1938, John 1982, Defrise and Liu 1999, Defrise et al. 2013). The two consistency equations (11), (12) and John's equation (15) for histo-images can be converted into the corresponding equations in the sinogram parameterization of the data in (1) (Defrise et al. 2013), and the details are shown in Appendix B.

The histo-image has an essentially bounded support because the object f has a bounded support and the kernel κ in (9) decays exponentially for a Gaussian TOF profile. So we can always use a Dirichlet/zero spatial boundary by selecting an image field-of-view larger than the object. From figure 1, we obtain the same TOF LOR by changing angles $\varphi\rightarrow\varphi+\pi$, $\theta\rightarrow-\theta$ and time $t\rightarrow-t$. So the consistent histo-images also satisfy the symmetry property

$$q(\vec{x},\hat{n}(\phi,\theta))=q(\vec{x},\hat{n}(\phi+\pi,-\theta))=q(\vec{x},-\hat{n}(\phi,\theta)). \quad (16)$$

2.3. An analytical solution for attenuation gradients

After correcting for scattered and random coincidences, we can model the expectation histo-image $m(x,\vec{n})\hat{}$ as

$$m(\vec{x},\hat{n})=a(\vec{x},\hat{n})q(\vec{x},\hat{n}), \quad (17)$$

where $a(x,\vec{n})\hat{}$ is the attenuation factor. Based on Beer-Lambert law, we can write the attenuation factor as

$$a(\vec{x},\hat{n})=\exp\left[-\int_{-\infty}^{\infty}\mathrm{d}l\mu(\vec{x}+l\hat{n})\right], \quad (18)$$

where $\mu(x)\vec{}$ is the linear attenuation coefficients. To simplify notations and derivations below, we use here the same histo-image parameterization for the attenuation factors and for

the emission data. Note however that the attenuation factor is independent of the TOF variable, i.e., it is constant along the TOF direction n, $\hat{a}(x,\vec{n})\hat{} = a(x \vec{+} ln,\hat{n})\hat{}$. So its directional derivative along n $\hat{\text{is}}$

$$\hat{n}\cdot\nabla a(\vec{x},\hat{n})=\frac{d}{dl}a(\vec{x}+l\hat{n},\hat{n})\Big|_{l=0}=0. \quad (19)$$

The attenuation corrected emission histo-image $q(x,\vec{n})\hat{}$ satisfies the consistency equations. Putting $q(x,\vec{n})\hat{} = m(x,\vec{n})\hat{/}a(x,\vec{n})\hat{}$ into (10), applying the chain rule and using (19), we obtain

$$\begin{aligned}0=\diamond\left(\frac{m(\vec{x},\hat{n})}{a(\vec{x},\hat{n})}\right)&=\frac{\diamond m(\vec{x},\hat{n})}{a(\vec{x},\hat{n})}+m(\vec{x},\hat{n})\diamond\frac{1}{a(\vec{x},\hat{n})}-\sigma^2(\hat{n}\cdot\nabla m(\vec{x},\hat{n}))\left(\nabla\frac{1}{a(\vec{x},\hat{n})}\right)\\&=\frac{\diamond m(\vec{x},\hat{n})}{a(\vec{x},\hat{n})}-\frac{m(\vec{x},\hat{n})}{a^2(\vec{x},\hat{n})}\nabla_{\hat{n}}a(\vec{x},\hat{n})+\sigma^2\frac{\hat{n}\cdot\nabla m(\vec{x},\hat{n})}{a^2(\vec{x},\hat{n})}\nabla a(\vec{x},\hat{n})\\&=\frac{\diamond m(\vec{x},\hat{n})}{a(\vec{x},\hat{n})}-\frac{m(\vec{x},\hat{n})}{a(\vec{x},\hat{n})}\nabla_{\hat{n}}\log a(\vec{x},\hat{n})+\sigma^2\frac{\hat{n}\cdot\nabla m(\vec{x},\hat{n})}{a(\vec{x},\hat{n})}\nabla\log a(\vec{x},\hat{n}).\end{aligned} \quad (20)$$

Multiplying the above equation by $a(x,\vec{n})\hat{}$, we obtain

$$m(\vec{x},\hat{n})\nabla_{\hat{n}}\log a(\vec{x},\hat{n})-\sigma^2\hat{n}\cdot\nabla m(\vec{x},\hat{n})\nabla\log a(\vec{x},\hat{n})=\diamond m(\vec{x},\hat{n}), \quad (21)$$

where $\diamond m(x,\vec{n})\hat{} = \nabla_n m(x,\vec{n})\hat{} - \sigma^2 n\hat{}\cdot\nabla\nabla m(x,\vec{n})\hat{}$. We would like to estimate the angular gradient $\nabla_n \log a$ and spatial gradient $\nabla \log a$ for a fixed LOR defined by a point $x_0\vec{}$ and a direction $n,\hat{}$ from the relevant data set $\{m(x_0\vec{} + ln,\hat{n})\hat{}|l \in \mathbb{R}\}$, which contains all TOF bins for this LOR. Along the TOF direction $n,\hat{}$ the attenuation factor $a(x_0\vec{}, n)\hat{}$ is unchanged, so its spatial gradient with respect to $x_0\vec{}$ is also unchanged,

$$\nabla a(\vec{x}_0+l\hat{n},\hat{n})=\nabla a(\vec{x}_0,\hat{n}). \quad (22)$$

To proceed, we define the angular gradient of $\log a(x_0\vec{} + ln,\hat{n})\hat{}$ as

$$\nabla_{\hat{n}}\log a(\vec{x}_0+l\hat{n},\hat{n})=\mathscr{D}_{\hat{n}}\log a(\vec{x}_0+l\hat{c},\hat{n})|_{\hat{c}=\hat{n}}, \quad (23)$$

where $\mathscr{D}_{\hat{n}}$ is the total angular gradient. Using the chain rule, we can then calculate the angular gradient $\nabla_n \log a(x_0\vec{} + ln,\hat{n})\hat{}$ as (Defrise et al. 2015)

$$\begin{aligned}\nabla_{\hat{n}}\log a(\vec{x}_0+l\hat{n},\hat{n})&=\mathscr{D}_{\hat{n}}\log a(\vec{x}_0+l\hat{n},\hat{n})-\mathscr{D}_{\hat{n}}\log a(\vec{x}_0+l\hat{n},\hat{c})|_{\hat{c}=\hat{n}}\\&=\mathscr{D}_{\hat{n}}\log a(\vec{x}_0,\hat{n})-l\nabla\log a(\vec{x}_0+l\hat{n},\hat{n})\\&=\nabla_{\hat{n}}\log a(\vec{x}_0,\hat{n})-l\nabla\log a(\vec{x}_0,\hat{n}).\end{aligned} \quad (24)$$

Here we used $\mathscr{D}_{\hat{n}} a(x_0\vec{} + ln,\hat{n})\hat{} = \mathscr{D}_{\hat{n}} a(x_0\vec{}, n)\hat{}$ since $a(x_0\vec{} + ln,\hat{n})\hat{} = a(x_0\vec{}, n)\hat{}$. Using (22) and (24), we can rewrite (21) at $x \vec{=} x_0\vec{} + ln$ $\hat{\text{as}}$

$$-[\sigma^2\hat{n}\cdot\nabla m+lm]\nabla\log a(\vec{x}_0,\hat{n})+m\nabla_{\hat{n}}\log a(\vec{x}_0,\hat{n})=\diamond m. \quad (25)$$

Here we have dropped the arguments $(\vec{x_0}+l\hat{n},\hat{n})$ of m for conciseness. Again, (25) can be interpreted as two basis equations along directions $\hat{u}$ and $\hat{v}$

$$-(\sigma^2\hat{n}\cdot\nabla m+lm)\,\hat{u}\cdot\nabla\log a(\vec{x}_0,\hat{n})+m\hat{u}\cdot\nabla_{\hat{n}}\log a(\vec{x}_0,\hat{n})=\hat{u}\cdot\diamond m. \quad (26)$$

$$-(\sigma^2\hat{n}\cdot\nabla m+lm)\,\hat{v}\cdot\nabla\log a(\vec{x}_0,\hat{n})+m\hat{v}\cdot\nabla_{\hat{n}}\log a(\vec{x}_0,\hat{n})=\hat{v}\cdot\diamond m. \quad (27)$$

For fixed $(\vec{x_0},\hat{n})$, the above equations hold for all measurements $m(\vec{x_0}+l\hat{n},\hat{n})$ with $\vec{x_0}\cdot\hat{n}+l\in T$, with T denoting the TOF interval where the data are measured. So one can solve (26) and (27) for the spatial/angular gradients in the least square sense (Defrise et al. 2012). For instance, the least square solution for $\hat{u}\cdot\nabla\log a(\vec{x_0},\hat{n})$ and $\hat{u}\cdot\nabla_n \log a(\vec{x_0},\hat{n})$ in (26) can be obtained by minimizing the Euclidean norm

$$\mathscr{E}=\int_T dl\left|\hat{u}\cdot\diamond m+(\sigma^2\hat{n}\cdot\nabla m+lm)\,\hat{u}\cdot\nabla\log a(\vec{x}_0,\hat{n})-m\hat{u}\cdot\nabla_{\hat{n}}\log a(\vec{x}_0,\hat{n})\right|^2. \quad (28)$$

After equating the derivatives with respect to the unknowns to zero, we obtain

$$\begin{bmatrix} H_{11} & H_{12} \\ H_{12} & H_{22} \end{bmatrix}\begin{bmatrix} -\hat{u}\cdot\nabla\log a(\vec{x}_0,\hat{n}) \\ \hat{u}\cdot\nabla_{\hat{n}}\log a(\vec{x}_0,\hat{n}) \end{bmatrix}=\begin{bmatrix} J_1 \\ J_2 \end{bmatrix} \quad (29)$$

where

$$H_{11}=\int_T dl(\sigma^2\hat{n}\cdot\nabla m+lm)^2,\ H_{12}=\int_T dl\,(\sigma^2\hat{n}\cdot\nabla m+lm)\,m,\ H_{22}=\int_T dlm^2,$$
$$J_1=\int_T dl\,(\sigma^2\hat{n}\cdot\nabla m+lm)\,\hat{u}\cdot\diamond m,\ J_2=\int_T dlm\hat{u}\cdot\diamond m. \quad (30)$$

Solving (29), we obtain the least-squares (LS) estimate

$$-\hat{u}\cdot\nabla\log a^{(\mathrm{est})}(\vec{x}_0,\hat{n})=\frac{H_{22}J_1-H_{12}J_2}{H_{11}H_{22}-H_{12}^2}, \quad (31)$$

$$\hat{u}\cdot\nabla_{\hat{n}}\log a^{(\mathrm{est})}(\vec{x}_0,\hat{n})=\frac{H_{11}J_2-H_{12}J_1}{H_{11}H_{22}-H_{12}^2}. \quad (32)$$

The above LS solution for histo-images is equivalent to equation (24) for the sinogram parameterization in (Defrise et al. 2012). Similar to the attenuation histo-image, the directional derivatives in the LS solution are also spatially invariant along the TOF direction, and the detailed verification is shown in Appendix C. Based on the Schwarz inequality, the matrix in (29) is positive-semidefinite for a fixed $(\vec{x_0},\hat{n})$; the denominator $H_{11}H_{22}-H_{12}^2$ is nonnegative and it becomes zero if and only if there is only one point source along the line $\{\vec{x_0}+l\hat{n}|l\in\mathbb{R}\}$ (Defrise et al. 2012). In this case, the two equations in (29) are dependent and there are infinitely many solutions. For an LOR tangent to the patient boundary, the solution is unstable since there is only one point having activity along the

LOR. In such case, one can use regularization to stabilize the solution by adding a regularization term in (28). For instance, one can use the Tikhonov regularization to obtain solutions with smaller norms by replacing H_{11} with $H_{11} + \beta_1$ and H_{22} with $H_{22} + \beta_2$, with hyperparameters β_1, β_2 to control the amount of regularization (Tikhonov and Arsenin 1977). It is worth noting that the directional derivatives $v \cdot \nabla \log a^{(\text{est})}(x_0, n)$ and $v \cdot \nabla_n \log a^{(\text{est})}(x_0, n)$ can also be solved using (30), (31) and (32) by replacing $\hat{u}$ with v.

2.4. Estimate attenuation from its directional derivatives

Methods to reconstruct shapes from gradient data (Southwell 1980, Ettl et al. 2008, Huang et al. 2015), can be used to reconstruct attenuation histo-images from their directional derivatives. However, the boundary conditions are not considered in these methods and the attenuation can only be determined up to an additive constant for $\log a(x, n)$, which amounts to a multiplicative constant for the attenuation factors and activity image. This constant can be estimated using boundary conditions dictated by the finite support of the object. Here we consider the 2D case with $\theta = 0$. We derive a fast dedicated method to uniquely determine attenuation histo-images (or sinograms) from their directional derivatives while explicitly considering the boundary conditions. For conciseness, we consider an azimuthal angular range $\varphi \in [0, 2\pi)$. In practice, histo-images only have range $\varphi \in [0, \pi)$; however, one can stack two replicates with one flipped along s by applying the symmetric property (16). Since attenuation is constant along the TOF direction n, and we can formulate the attenuation as $\mathcal{R}\mu(s, \varphi) = -\log a(x, n)$ with $s = x \cdot \hat{u}$, $x \cdot n = 0$, $n = (-\sin \varphi, \cos \varphi)$ and $\hat{u} = (\cos \varphi, \sin \varphi)$. Applying (13) and (B.3), we have the following partial derivatives

$$\frac{\partial}{\partial s}\mathcal{R}\mu(s,\phi) = -\hat{u} \cdot \nabla \log a(\vec{x}, \hat{n}), \qquad \frac{\partial}{\partial \phi}\mathcal{R}\mu(s,\phi) = \hat{u} \cdot \nabla_{\hat{n}} \log a(\vec{x}, \hat{n}). \quad (33)$$

The above equation is always implemented numerically to estimate the digitized version of $\mathcal{R}\mu(s, \varphi)$. We use N_s and N_φ to denote the number of samples, Δ_s and Δ_φ to denote the sampling intervals, along s and φ, respectively. We use vectorization $\text{vec}(\boldsymbol{A})$ for a matrix $\boldsymbol{A}$ to denote a column vector obtained by stacking the columns of $\boldsymbol{A}$, e.g. we use $\text{vec}(\mathcal{R}\boldsymbol{\mu}) \in \mathbb{R}^{N_s N_\varphi}$ to denote the digitized version of attenuation $\mathcal{R}\mu(s, \varphi)$. The finite difference can be used to approximate the partial derivatives in (33) with zero boundary along s and periodic boundary along φ. We use higher order terms in the Taylor series (exact up to the 4-th order) to approximate the difference using the directional derivatives (Li et al. 2013a). We use the vectorized forms for the attenuation sinogram and the derivatives and rewrite (33) in matrix form

$$\begin{bmatrix} \boldsymbol{I}_\phi \otimes \boldsymbol{D}_s \\ \boldsymbol{D}_\phi \otimes \boldsymbol{I}_s \end{bmatrix} \text{vec}(\mathcal{R}\boldsymbol{\mu}) = \begin{bmatrix} \Delta_s \boldsymbol{I}_\phi \otimes \boldsymbol{M}_s \text{vec}(-\hat{u} \cdot \nabla \log \boldsymbol{a}) \\ \Delta_\phi \boldsymbol{M}_\phi \otimes \boldsymbol{I}_s \text{vec}(\hat{u} \cdot \nabla_{\hat{n}} \log \boldsymbol{a}) \end{bmatrix}, \quad (34)$$

where $\boldsymbol{I}_s$, $\boldsymbol{I}_\varphi$ are $N_s \times N_s$ and $N_\varphi \times N_\varphi$ identity matrices, $\boldsymbol{D}_s$ and $\boldsymbol{D}_\varphi$ are $(N_s + 1) \times N_s$ and $N_\varphi \times N_\varphi$ difference matrices given by

$$\boldsymbol{D}_s=\begin{bmatrix} 1 & & & \\ -1 & 1 & & \\ & -1 & \ddots & \\ & & \ddots & 1 \\ & & & -1 \end{bmatrix}, \quad \boldsymbol{D}_\phi=\begin{bmatrix} -1 & 1 & & \\ & -1 & \ddots & \\ & & \ddots & 1 \\ 1 & & & -1 \end{bmatrix}, \tag{35}$$

and $(N_s + 1) \times N_s$ matrix $\boldsymbol{M}_s$ and $N_\varphi \times N_\varphi$ matrix $\boldsymbol{M}_\varphi$ are given by (Adapted from equation (9) in (Li et al. 2013a) after considering boundary condition)

$$\boldsymbol{M}_s=\frac{1}{24}\begin{bmatrix} 13 & -1 & & \\ 13 & 13 & \ddots & \\ -1 & 13 & \ddots & -1 \\ & \ddots & \ddots & 13 \\ & & -1 & 13 \end{bmatrix}, \quad \boldsymbol{M}_\phi=\frac{1}{24}\begin{bmatrix} 13 & 13 & -1 & & -1 \\ -1 & 13 & 13 & \ddots & \\ & -1 & 13 & \ddots & -1 \\ -1 & & \ddots & \ddots & 13 \\ 13 & -1 & & -1 & 13 \end{bmatrix}. \tag{36}$$

Here we used the Kronecker product $\otimes$ for block matrix operations. The Dirichlet boundary condition $\mathscr{R}\boldsymbol{\mu} = 0$ at the edge of the s range, is reflected by the first and last rows of $\boldsymbol{D}_s$ and $\boldsymbol{M}_s$; the periodic boundary along φ is reflected by the circulant matrices $\boldsymbol{D}_\varphi$ and $\boldsymbol{M}_\varphi$. Equation (34) is overdetermined since there are $(2N_s + 1)N_\varphi$ equations but N_sN_φ unknowns in attenuation $\mathscr{R}\boldsymbol{\mu}$. The attenuation can be estimated in the least-squares sense by solving

$$(\boldsymbol{I}_\phi \otimes \boldsymbol{K}_s + C_\phi \otimes \boldsymbol{I}_s)\,\mathrm{vec}(\mathscr{R}\boldsymbol{\mu}) = \mathrm{vec}(\boldsymbol{G}), \tag{37}$$

where

$$\boldsymbol{G} = \Delta_s \boldsymbol{D}_s^T\, \boldsymbol{M}_s(-\hat{u}\cdot\nabla \log \boldsymbol{a}) + \Delta_\phi(\hat{u}\cdot\nabla_{\hat{n}}\log \boldsymbol{a})\boldsymbol{M}_\phi^T\, \boldsymbol{D}_\phi, \tag{38}$$

and the symmetric tridiagonal matrix $\boldsymbol{K}_s$ and circulant matrix $\boldsymbol{C}_\varphi$ are given by

$$\boldsymbol{K}_s=\boldsymbol{D}_s^T\,\boldsymbol{D}_s=\begin{bmatrix} 2 & -1 & & \\ -1 & 2 & \ddots & \\ & \ddots & \ddots & -1 \\ & & -1 & 2 \end{bmatrix}, \quad \boldsymbol{C}_\phi=\boldsymbol{D}_\phi^T\,\boldsymbol{D}_\phi=\begin{bmatrix} 2 & -1 & & -1 \\ -1 & 2 & \ddots & \\ & \ddots & \ddots & -1 \\ -1 & & -1 & 2 \end{bmatrix}. \tag{39}$$

Here we used the matrix equation $\mathrm{vec}(\boldsymbol{ABC}) = (\boldsymbol{C}^T \otimes \boldsymbol{A})\mathrm{vec}(\boldsymbol{B})$ in (38) (Horn and Johnson 1994). The matrix $(\boldsymbol{I}_\varphi \otimes \boldsymbol{K}_s + \boldsymbol{C}_\varphi \otimes \boldsymbol{I}_s)$ in (37) is positive definite due to the positive-definite matrix $\boldsymbol{K}_s$ and positive semidefinite matrix $\boldsymbol{C}_\varphi$ (Strang 2007), so (37) has a unique solution for attenuation estimation. One can use the Gauss-Seidel method or Jacobi method to solve (37), and the diagonal elements of $(\boldsymbol{I}_\varphi \otimes \boldsymbol{K}_s + \boldsymbol{C}_\varphi \otimes \boldsymbol{I}_s)$ are all equal to 4 (Southwell 1980). Noting that (37) is the vectorization form of Sylvester equation $\boldsymbol{K}_s\mathscr{R}\boldsymbol{\mu} + \mathscr{R}\boldsymbol{\mu}\boldsymbol{C}_\phi^T = \boldsymbol{G}$, one can also use the Sylvester equation solver to solve (37). Here, we use the special property of

sparse matrices $\boldsymbol{K}_s$ and $\boldsymbol{C}_\varphi$ to derive a dedicated fast solver for (37). The matrix $\boldsymbol{K}_s$ can be diagonalized by the discrete sine transform and $\boldsymbol{C}_\varphi$ can be diagonalized by the fast Fourier transform (Strang 2007)

$$\boldsymbol{K}_s=\mathscr{S}^{-1}\mathrm{diag}(\boldsymbol{\lambda}_s)\mathscr{S}, \quad \boldsymbol{C}_\phi=\mathscr{F}^{-1}\mathrm{diag}(\boldsymbol{\lambda}_\phi)\mathscr{F}, \quad (40)$$

where **S** is the discrete sine transform matrix/operator, and $\mathscr{F}$ is the fast Fourier transform (FFT) matrix/operator, and the eigenvalues are

$$[\boldsymbol{\lambda}_s]_k=2-2\cos\frac{k\pi}{N_s+1}, k=1,2,\ldots,N_s, \quad (41)$$

$$[\boldsymbol{\lambda}_\phi]_\ell=2-2\cos\frac{2\pi\ell}{N_\phi}, \ell=0,1,\ldots,N_\phi-1. \quad (42)$$

Applying (40)–(42), we obtain following fast attenuation solver/estimator

$$\mathscr{R}\boldsymbol{\mu}^{(\mathrm{est})}=\mathscr{S}^{-1}\left(\frac{\mathscr{S}\boldsymbol{G}\mathscr{F}^{-1}}{\boldsymbol{\lambda}_s\oplus\boldsymbol{\lambda}_\phi}\right)\mathscr{F}. \quad (43)$$

We used Hadamard element-wise division and Kronecker sum $\oplus$ for convenience, the $k\ell$-th element $[\boldsymbol{\lambda}_s\oplus\boldsymbol{\lambda}_\varphi]_{k\ell}=[\boldsymbol{\lambda}_s]_k+[\boldsymbol{\lambda}_\varphi]_\ell$. We can apply the discrete sine transform along s and fast Fourier transform along φ in the implementation of (43), and the computational complexity is $O(N_sN_\varphi\log(N_sN_\varphi))$. The fast dedicated solver (43) shares the same spirit as the fast Poisson solver in solving the Poisson equation (Strang 2007).

3. Numerical example

3.1. Simulation setup and XCAT phantom

To evaluate the attenuation estimation from TOF-PET data, we simulated a generic 2D TOF-PET system with 4mm crystals. A 2D TOF-PET projector was implemented using a strip-integral model with a Gaussian TOF profile with spatial FWHM of 75 mm, which corresponds to a timing resolution of about 500 ps FWHM. We used 41 TOF bins with bin size of 24 mm. The histo-images were generated by back-projecting the TOF sinograms for each angle using (4). The histo-image has 180 azimuthal angles uniformly spaced over 180°. To reduce the truncation in the convolution of the histo-image with the elongated TOF kernel, we used a large histo-image of 176 × 176 with 4mm pixel size. We used the XCAT phantom (formerly known as NCAT) (Segars and Tsui 2009, Li 2011), and the activity and attenuation images are shown in figure 2. Since the estimate of derivatives for LORs tangent to the object boundary is inaccurate, we added an external ring source containing 6.9% of body activity with diameter of 57.6 cm (Mollet et al. 2012, Mollet et al. 2014, Panin et al. 2013). The ring source allows an accurate estimate of derivatives for these LORs because it adds two activity points along each LOR passing through the scanner's FOV.

Figure 3 shows the histo-image generation along the direction $\hat{n}$ at $\varphi = 135°$. The expectation TOF sinogram $p(t, s, \varphi)$ ($z = 0$, $\theta = 0$ for this 2D simulation and these arguments are omitted) was obtained using the TOF-PET projector. The attenuation factors are obtained by taking the exponential of the negative of the integral of the attenuation image $\mu(x)$ along $\hat{n}$, as formulated in (18). The attenuated TOF sinogram in figure 3(d) was obtained by taking the product of $p(t, s, \varphi)$ and the corresponding attenuation factor. The noisy TOF sinogram was generated by applying a Poisson random generator to the attenuated TOF sinogram, and then the noisy histo-image $m(x, \hat{n})$ was obtained from the noisy TOF sinogram by convolving it with the kernel h_B according to (4). We simulated three different noise levels—noise-free and two noise levels. The total numbers of expected events in the histo-image are 4×10^6 and 1×10^6 for the moderate and the high noise cases, respectively. The attenuation derivatives estimated from noisy CW histo-images were always found to be more accurate than those estimated from noisy MLA histo-images. Therefore, we selected CW histo-images instead of MLA histo-images in the rest of this section.

3.2. Estimate directional derivatives of attenuation histo-image

The directional derivatives can be estimated using the LS method in (31) and (32), and we have $\theta = 0$ in the 2D case considered for our simulation. The derivatives are invariant along TOF direction $\hat{n}$, so we can estimate the coefficients in (30) for all $x_0 = s\hat{u}$. The line integrations over l in (30) can be naturally implemented as forward projections of the integrands formatted as histo-images along each direction $\hat{n}$. The directional derivatives $\hat{n} \cdot \nabla m(x, \hat{n})$ was approximated as a convolution with $[1/2, 0, -1/2]/\Delta$ with bin size Δ. Applying (13), we can approximate $\hat{u} \cdot \nabla_n m(x, \hat{n})$ using the central difference along φ. The least-square estimate of the gradients of the attenuation can be unstable for LORs having weak activity, which is a concern in particular for the LORs tangent to the ring source. To improve robustness to noise we regularized the gradient calculation in (31) and (32), as explained at the end of Section 2.3. The regularization parameters β_1 and β_2 were set equal to 10% of the minimum values of H_{11} and H_{22} in a central region of the histo-image (or sinogram). To avoid introducing bias for the LORs containing sufficient activity, regularization was applied only for LORs such that $H_{11} < \beta_1$ or $H_{22} < \beta_2$. The estimated directional derivatives $-\hat{u} \cdot \nabla \log \boldsymbol{a}$ and $\hat{u} \cdot \nabla_n \log \boldsymbol{a}$ are shown in figure 4. The approximation of the true derivatives using the central difference is also shown for comparison.

3.3. Estimate attenuation sinograms and reconstructed attenuation images

We used the central region of 54.4 cm (fully covering patient or “the activity phantom”) in estimating the attenuation sinogram to remove the unstable values in the estimated directional derivatives near the ring source in figure 4. The attenuation sinograms estimated from the directional derivatives in figure 4 using the fast solver (43) are shown in figure 5. Figure 6 shows a horizontal profile through the four sinograms at $\varphi = 135°$ of figure 5. The underestimation for the noisy cases can be attributed to the nonlinearity in the gradient estimation with respect to the noisy histo-image $m(x, \hat{n})$. The bias can be reduced by direct attenuation estimation, e.g. (Li et al. 2013b).

We also present the reconstructed attenuation images $\mu(\vec{x})$ to demonstrate the performance of the attenuation estimation in figure 7. The reconstruction of attenuation image is not required for PET attenuation correction. For comparison, we also show the reference images obtained by assuming that the true activity distribution in figure 2(a) was known. In this case, the attenuation reconstruction reduces to that in transmission tomography with a virtual blank scan equal to the true activity sinogram. The reference attenuation images were reconstructed using filtered back projection (FBP) and MLTR, a maximum-likelihood algorithm dedicated to transmission tomography (Nuyts et al. 1998). We used 12 iterations with 20 ordered-subsets in the MLTR reconstructions. We also used the FBP to reconstruct the attenuation image from the estimated sinograms. We smoothed the attenuation sinogram with a moving average kernel $[1/3, 1/3, 1/3]^T$ applied along s to reduce noise in both the estimated and FBP reconstructions. There is a small crosstalk artifact (barely visible) from the activity in the heart region in the noise-free reconstructed attenuation images and the two reference images reconstructed using FBP and MLTR in figure 7. This artifact is attributed to the leaking of activity signal into the attenuation sinogram.

4. Discussion

TOF-PET data can be naturally stored in histo-image format without information loss, and the DIRECT approach can be used for very efficient 3D TOF PET Reconstruction (Matej et al. 2009, Daube-Witherspoon et al. 2012). The attenuation histo-image formation allows estimating the attenuation directly from the selected data parameterization (histo-images) without having to first rebin to sinograms. The TOF-PET histo-image (or sinogram) has two degrees of redundancy; we formulated two consistency equations to characterize the redundancy. Thanks to the histo-image parameterization, the consistency equations in histo-image format are more concise and elegant than the consistency equations in the sinogram format, and they provide a better insight into the rich structure of TOF-PET data.

Consistency equations can also be derived in Fourier space, and again the histo-image parameterization leads to an elegant vector formulation independent of the coordinate system used. These equations are given in Appendix A. Equation (A.4) can be used to develop fast Fourier-based forward- and back-projectors for iterative image reconstruction (Matej et al. 2004, Cho et al. 2007), and to develop Fourier rebinning for TOF-PET histo-images, e.g., mapping the 3D TOF histo-images to 2D TOF histo-images (Defrise et al. 2005, Cho et al. 2009). The consistency equations for histo-image can also be applied to estimate the missing data in TOF PET due to incomplete linear or angular sampling due to, e.g., detector gaps (Karp et al. 1988).

Previously, it was showed that TOF-PET data determine attenuation sinograms up to a constant (Defrise et al. 2012). We developed a transmission-less attenuation estimation algorithm based on the consistency equations and showed from theory and an example that the attenuation histo-image (or sinogram) can be uniquely estimated from the TOF-PET histo-images when the time-of-flight (TOF) information is available. In principle, the attenuation can be fully determined from its directional derivatives, and the scaling constant is naturally solved by considering the boundary conditions. However, since the estimate of the directional derivatives of the attenuation is inaccurate for LORs tangent to object

boundary, an external source might be needed to give accurate estimate for such LORs (Mollet et al. 2012, Mollet et al. 2014). The comparison of the directional derivatives estimated with and without ring source in figure 8, shows that the estimated derivatives are inaccurate for LORs tangent to the patient boundary when no ring source is used. After adding the ring source (considered as part of the entire activity during reconstruction), the inaccurate values move from the LORs tangent to patient to the LORs tangent to ring source. The LORs tangent to the ring source do not intersect the patient, and these errors do not affect the patient activity reconstruction. The ring or annulus source is not needed during the entire scan, so one can use a rotating point or line source (Panin et al. 2013). One can also use the source rotation with cardiac and respiratory gating for attenuation and activity estimation across gating frames. It is worth noting that one can also use the proposed attenuation estimation method to estimate the normalization factors for TOF PET with known attenuation (Rezaei et al. 2014). In this case, the external source can be removed, and the inaccurate values can be obtained using a model-based extrapolation method.

How to optimally extract all the attenuation-related information from TOF-PET histo-images is still an open question, and it is beyond of the scope of this paper. The reconstruction incorporating all physics effects and modeling of Poisson noise is likely to produce superior image quality in the reconstructed attenuation image, e.g., the maximum-likelihood reconstruction for TOF-PET with simultaneous estimation of activity and the attenuation factors (MLACF) (Defrise et al. 2014, Rezaei et al. 2014). However, the joint maximum-likelihood estimation of activity and attenuation is not a convex optimization, and the estimation may not converge to the desired solution but to a saddle point or a local maximum. In this case, the fast analytic attenuation estimation can be used as initial sinogram/histo-image for MLACF which allows the MLACF converge to the desired solution. For 2D TOF PET, there is only one degree of redundancy, and we used only (26) to calculate the 2D directional derivatives in (31) and (32). For 3D TOF PET, there are two degrees of redundancy, and we can use both (26) and (27) to calculate the 4D directional derivatives—$\hat{u} \cdot \nabla \log a^{(\text{est})}$, $\hat{u} \cdot \nabla_n \log a^{(\text{est})}$, $v \cdot \nabla \log a^{(\text{est})}$ and $v \cdot \nabla_n \log a^{(\text{est})}$, and then estimate attenuation from these derivatives. An alternative method is to estimate attenuation directly from (26) and (27) for 3D TOF PET. An efficient implementation of attenuation estimation for 3D TOF PET utilizing all measurement data needs to be investigated, which is our future work.

5. Conclusion

We developed an attenuation-estimation method for fully 3D TOF-PET emission histo-images with pre-correction of scattered and random coincidences. The attenuation estimation from histo-images is not only a theoretical result, but has a practical impact. It can provide better insight into the problem of simultaneous activity and attenuation estimation in TOF PET. The numerical example showed that the attenuation histo-images or sinograms can be uniquely estimated from the 2D TOF-PET emission histo-images with an external ring source. Future work will extend this work to 3D TOF-PET to efficiently estimate attenuation histo-images (or sinograms) utilizing all measured TOF-PET data.

Acknowledgments

Research reported in this paper was supported in part by the National Institute of Biomedical Imaging and Bioengineering (NIBIB) and the National Cancer Institute (NCI) of the National Institutes of Health (NIH) under award numbers R21EB017416, R01EB002131 and R01CA113941. This work was also supported by project G027514N of the Research Foundation Flanders (FWO) and by the SRP 10 project of the Vrije Universiteit Brussel. The content is solely the responsibility of the authors and does not necessarily represent the official views of the National Institutes of Health.

References

Burgos N, Cardoso MJ, Thielemans K, Modat M, Pedemonte S, Dickson J, Barnes A, Ahmed R, Mahoney CJ, Schott JM, Duncan JS, Atkinson D, Arridge SR, Hutton BF, Ourselin S. Attenuation correction synthesis for hybrid PET-MR scanners: Application to brain studies. IEEE Trans Med Imag. 2014; 33(12):2332–2341.

Cho S, Ahn S, Li Q, Leahy RM. Exact and approximate Fourier rebinning of PET data from time-of-flight to non time-of-flight. Phys Med Biol. 2009; 54(3):467–484. [PubMed: 19124956]

Cho S, Li Q, Ahn S, Bai B, Leahy RM. Iterative image reconstruction using inverse Fourier rebinning for fully 3-D PET. IEEE Trans Med Imag. 2007; 26(5):745–756.

Daube-Witherspoon ME, Matej S, Werner ME, Surti S, Karp JS. Comparison of list-mode and DIRECT approaches for time-of-flight PET reconstruction. IEEE Trans Med Imag. 2012; 31(7): 1461–1471.

Daube-Witherspoon ME, Surti S, Perkins A, Kyba CCM, Wiener R, Werner ME, Kulp R, Karp JS. The imaging performance of a $LaBr_3$-based PET scanner. Phys Med Biol. 2010; 55(1):45–64. [PubMed: 19949259]

Defrise M, Casey M, Michel C, Conti M. Fourier rebinning of time-of-flight PET data. Phys Med Biol. 2005; 50(12):2749–2763. [PubMed: 15930600]

Defrise, M.; Li, Y.; Matej, S. Consistency equation for TOF-PET histo-images: derivation and applications. 13th Int. Conf. on Fully 3D image Reconstruction in Radiology and Nuclear Medicine; Newport, RI. 2015. p. 280-3.

Defrise M, Liu X. A fast rebinning algorithm for 3D positron emission tomography using John's equation. Inverse Problems. 1999; 15(4):1047–1065.

Defrise M, Panin V, Michel C, Casey ME. Continuous and discrete data rebinning in time-of-flight PET. IEEE Trans Med Imag. 2008; 27(9):1310–1322.

Defrise M, Panin VY, Casey ME. New consistency equation for time-of-flight PET. IEEE Trans Nucl Sci. 2013; 60(1):124–133.

Defrise M, Rezaei A, Nuyts J. Time-of-flight PET data determine the attenuation sinogram up to a constant. Phys Med Biol. 2012; 57(4):885–899. [PubMed: 22290428]

Defrise M, Rezaei A, Nuyts J. Transmission-less attenuation correction in time-of-flight PET: analysis of a discrete iterative algorithm. Phys Med Biol. 2014; 59(4):1073–1095. [PubMed: 24504259]

Ettl S, Kaminski J, Knauer MC, Häusler G. Shape reconstruction from gradient data. Appl Opt. 2008; 47(12):2091–2097. [PubMed: 18425183]

Gould KL, Pan T, Loghin C, Johnson NP, Guha A, Sdringola S. Frequent diagnostic errors in cardiac PET/CT due to misregistration of CT attenuation and emission PET images: A definitive analysis of causes, consequences, and corrections. J Nucl Med. 2007; 48(7):1112–1121. [PubMed: 17574974]

Hofmann M, Bezrukov I, Mantlik F, Aschoff P, Steinke F, Beyer T, Pichler BJ, Schoelkopf B. MRI-based attenuation correction for whole-body PET/MRI: Quantitative evaluation of segmentation- and atlas-based methods. J Nucl Med. 2011; 52(9):1392–1399. [PubMed: 21828115]

Horn, RA.; Johnson, CR. Topics in Matrix Analysis. Cambridge University Press; Cambridge, UK: 1994.

Huang L, Idir M, Zuo C, Kaznatcheev K, Zhou L, Asundi A. Comparison of two-dimensional integration methods for shape reconstruction from gradient data. Optics and Lasers in Engineering. 2015; 64:1–11.

John F. The ultrahyperbolic differential equation with four independent variables. Duke Math J. 1938; 4(2):300–322.

John, F. Partial Differential Equations. 4. Springer-Verlag; New York, NY: 1982.

Karp JS, Muehllehner G, Lewitt R. Constrained Fourier space method for compensation of missing data in emission computed tomography. IEEE Trans Med Imag. 1988; 7(1):21–25.

Karp JS, Surti S, Daube-Witherspoon ME, Muehllehner G. Benefit of time-of-flight in PET: Experimental and clinical results. J Nucl Med. 2008; 49(3):462–470. [PubMed: 18287269]

Keereman V, Mollet P, Berker Y, Schulz V, Vandenberghe S. Challenges and current methods for attenuation correction in PET/MR. Magn Reson Mater Phy. 2013; 26(1):81–98.

Kinahan P, Townsend D, Beyer T, Sashin D. Attenuation correction for a combined 3D PET/CT scanner. Med Phys. 1998; 25(10):2046–2053. [PubMed: 9800714]

Li G, Li Y, Liu K, Ma X, Wang H. Improving wavefront reconstruction accuracy by using integration equations with higher-order truncation errors in the southwell geometry. J Opt Soc Am A. 2013a; 30(7):1448–1459.

Li, H.; El Fakhri, G.; Li, Q. Direct MAP estimation of attenuation sinogram using TOF PET data and anatomical image. 12th Int. Meeting on Fully 3-D Image Reconstruction in Radiology and Nuclear Medicine; Lake Tahoe, CA. 2013b. p. 404-407.

Li Y. Noise propagation for iterative penalized-likelihood image reconstruction based on Fisher information. Phys Med Biol. 2011; 56(4):1083–1103. [PubMed: 21263172]

Li, Y.; Defrise, M.; Metzler, SD.; Matej, S. Attenuation estimation from time-of-flight PET histoimages using consistency equations. 13th Int. Conf. on Fully 3D image Reconstruction in Radiology and Nuclear Medicine; Newport, RI. 2015. p. 95-8.

Liu X, Defrise M, Michel C, Sibomana M, Comtat C, Kinahan P, Townsend D. Exact rebinning methods for three-dimensional PET. IEEE Trans Med Imag. 1999; 18(8):657–664.

Martinez-Möller A, Souvatzoglou M, Delso G, Bundschuh RA, Chefd'hotel C, Ziegler SI, Navab N, Schwaiger M, Nekolla SG. Tissue classification as a potential approach for attenuation correction in whole-body PET/MRI: Evaluation with PET/CT data. J Nucl Med. 2009; 50(4):520–526. [PubMed: 19289430]

Matej S, Fessler JA, Kazantsev IG. Iterative tomographic image reconstruction using Fourier-based forward and back-projectors. IEEE Trans Med Imag. 2004; 23(4):401–412.

Matej S, Surti S, Jayanthi S, Daube-Witherspoon ME, Lewitt RM, Karp JS. Efficient 3-D TOF PET reconstruction using view-grouped histo-images: DIRECT–direct image reconstruction for TOF. IEEE Trans Med Imag. 2009; 28(5):739–751.

Mollet P, Keereman V, Bini J, Izquierdo-Garcia D, Fayad ZA, Vandenberghe S. Improvement of attenuation correction in time-of-flight PET/MR imaging with a positron-emitting source. J Nucl Med. 2014; 55(2):329–336. [PubMed: 24434291]

Mollet P, Keereman V, Clementel E, Vandenberghe S. Simultaneous MR-compatible emission and transmission imaging for PET using time-of-flight information. IEEE Trans Med Imag. 2012; 31(9):1734–1742.

Nuyts J, De Man B, Dupont P, Defrise M, Suetens P, Mortelmans L. Iterative reconstruction for helical CT: a simulation study. Phys Med Biol. 1998; 43(4):729–737. [PubMed: 9572499]

Panin VY, Aykac M, Casey ME. Simultaneous reconstruction of emission activity and attenuation coefficient distribution from TOF data, acquired with external transmission source. Phys Med Biol. 2013; 58(11):3649–3669. [PubMed: 23648397]

Rezaei A, Defrise M, Bal G, Michel C, Conti M, Watson C, Nuyts J. Simultaneous reconstruction of activity and attenuation in time-of-flight PET. IEEE Trans Med Imag. 2012; 31(12):2224–2233.

Rezaei A, Defrise M, Nuyts J. ML-reconstruction for TOF-PET with simultaneous estimation of the attenuation factors. IEEE Trans Med Imag. 2014; 33(7):1563–1572.

Segars WP, Tsui BMW. MCAT to XCAT: The evolution of 4-D computerized phantoms for imaging research. Proc IEEE. 2009; 97(12):1954–1968.

Snyder, DL.; Miller, MI. Random Point Processes in Time and Space. 2. Springer-Verlag; New York, NY: 1991.

Snyder DL, Thomas LJ Jr, Ter-Pogossian MM. A mathematical model for positron-emission tomography systems having time-of-flight measurements. IEEE Trans Nucl Sci. 1981; 28(3): 3575–3583.

Southwell WH. Wave-front estimation from wave-front slope measurements. J Opt Soc Amer. 1980; 70(8):998–1009.

Strang, G. Computational Science and Engineering. Wellesley-Cambridge Press; Wellesley, MA: 2007.

Surti S, Kuhn A, Werner ME, Perkins AE, Kolthammer J, Karp JS. Performance of philips gemini TF PET/CT scanner with special consideration for its time-of-flight imaging capabilities. J Nucl Med. 2007; 48(3):471–480. [PubMed: 17332626]

Tikhonov, AN.; Arsenin, VY. Solution of Ill-posed Problems. Winston & Sons; Washington, DC: 1977.

Wagenknecht G, Kaiser HJ, Mottaghy FM, Herzog H. MRI for attenuation correction in PET: methods and challenges. Magn Reson Mater Phy. 2013; 26(1):99–113.

Watson CC. An evaluation of image noise variance for time-of-flight PET. IEEE Trans Nucl Sci. 2007; 54(5):1639–1647.

Zaidi H, Ojha N, Morich M, Griesmer J, Hu Z, Maniawski P, Ratib O, Izquierdo-Garcia D, Fayad ZA, Shao L. Design and performance evaluation of a whole-body Ingenuity TF PET-MRI system. Phys Med Biol. 2011; 56(10):3091–3106. [PubMed: 21508443]

Appendix A. An alternative proof of consistency equation (10)

We first prove that the TOF kernel $\kappa(x,\vec{n})\hat{}$ satisfies (10). The TOF kernel is just the histo-image obtained from a point source $f(x)\vec{} = \delta(x)\vec{}$. The TOF kernel $\kappa(x,\vec{n})\hat{}$ is given by the following inverse Fourier transform (Watson 2007)

$$\kappa(\vec{x},\hat{n}) = \frac{1}{(2\pi)^3}\int_{\mathbb{R}^3} e^{-\sigma^2(\vec{\omega}\cdot\hat{n})^2/2} e^{j\vec{\omega}\cdot\vec{x}}\,\mathrm{d}^3\vec{\omega} = \mathscr{F}^{-1}\left[e^{-\sigma^2(\vec{\omega}\cdot\hat{n})^2/2}\right]. \quad \text{(A.1)}$$

Applying the derivative property of the Fourier transform (strictly speaking, in the distribution sense), we have

$$\nabla_{\hat{n}}\kappa(\vec{x},\hat{n}) = \mathscr{F}^{-1}\left[-\sigma^2\hat{n}\cdot\vec{\omega}\,\vec{\omega}\,e^{-\sigma^2(\vec{\omega}\cdot\hat{n})^2/2}\right], \quad \text{(A.2)}$$

$$\hat{n}\cdot\nabla\nabla\kappa(\vec{x},\hat{n}) = \mathscr{F}^{-1}\left[-\hat{n}\cdot\vec{\omega}\,\vec{\omega}\,e^{-\sigma^2(\vec{\omega}\cdot\hat{n})^2/2}\right]. \quad \text{(A.3)}$$

Using (A.2) and (A.3), we prove the TOF kernel $\kappa(x,\vec{n})\hat{}$ satisfies (10). Then we can prove any histo-image satisfies (10) using the fact that convolution commutes with differentiation.

In addition, we can write the Fourier transform of histo-image $q(x,\vec{n})\hat{}$ using the convolution theorem as

$$\hat{q}(\vec{\omega},\hat{n}) = \int_{\mathbb{R}^3} q(\vec{x},\hat{n}) e^{-j\vec{\omega}\cdot\vec{x}}\,\mathrm{d}^3\vec{x} = \hat{f}(\vec{\omega}) e^{-\sigma^2(\vec{\omega}\cdot\hat{n})^2/2}, \quad \text{(A.4)}$$

where $q(\vec{\omega})\hat{}$ is the Fourier transform of the object $f(x)\vec{}$. Equation (A.4) is the generalized projection slice theorem for 3D TOF-PET histo-image (Liu et al. 1999, Cho et al. 2009). By

taking the Fourier transform of (10) with respect to x, we can obtain the Fourier consistency equation in vector calculus form as

$$\hat{\diamond}\hat{q}(\vec{\omega},\hat{n})=\nabla_{\hat{n}}\hat{q}(\vec{\omega},\hat{n})+\sigma^2\hat{n}\cdot\vec{\omega}\vec{\omega}\hat{q}(\vec{\omega},\hat{n})=0. \quad \text{(A.5)}$$

where $\hat{\diamond}=\nabla_n+\sigma^2 n\hat{\cdot}\vec{\omega}\vec{\omega}$. One can verify that (A.4) is just the solution to (A.5).

Appendix B. Link with sinogram consistency equations

Histo-images and sinograms are connected by (4). Here we show that the histo-image consistency equations can be converted to consistency equations in sinogram format. By taking the inner product of x in (3) with the unit vectors $n, \hat{u}, v, \hat{}$ we can derive

$$t=\vec{x}\cdot\hat{n}+\tan\theta\vec{x}\cdot\hat{v},\ s=\vec{x}\cdot\hat{u},\ z=-\sec\theta\vec{x}\cdot\hat{v}. \quad \text{(B.1)}$$

We can use (B.1) and rewrite the gradient ∇ as

$$\begin{aligned}\nabla&=\nabla(\vec{x}\cdot\hat{n}+\tan\theta\vec{x}\cdot\hat{v})\frac{\partial}{\partial t}+\nabla(\vec{x}\cdot\hat{u})\frac{\partial}{\partial s}+\nabla(-\sec\theta\vec{x}\cdot\hat{v})\frac{\partial}{\partial z}\\&=(\hat{n}+\tan\theta\hat{v})\frac{\partial}{\partial t}+\hat{u}\frac{\partial}{\partial s}-\sec\theta\hat{v}\frac{\partial}{\partial z}.\end{aligned} \quad \text{(B.2)}$$

From (B.2), we can obtain the directional derivatives

$$\hat{n}\cdot\nabla=\frac{\partial}{\partial t},\ \hat{u}\cdot\nabla=\frac{\partial}{\partial s},\ \hat{v}\cdot\nabla=\tan\theta\frac{\partial}{\partial t}-\sec\theta\frac{\partial}{\partial z}. \quad \text{(B.3)}$$

Using (13) and (B.1), we can rewrite the first term of (11) with a $-\cos\theta$ factor as

$$\begin{aligned}&-\cos\theta\hat{u}\cdot\nabla_{\hat{n}}q(\vec{x},\hat{n})=\frac{d}{d\phi}p(t,s,\phi,z,\theta)\big|_{\vec{x}}\\&=\frac{\partial p}{\partial\phi}+\frac{\partial(\vec{x}\cdot\hat{u})}{\partial\phi}\big|_{\vec{x}}\frac{\partial p}{\partial s}+\frac{\partial(\vec{x}\cdot\hat{n}+\tan\theta\vec{x}\cdot\hat{v})}{\partial\phi}\big|_{\vec{x}}\frac{\partial p}{\partial t}+\frac{\partial(-\sec\theta\vec{x}\cdot\hat{v})}{\partial\phi}\big|_{\vec{x}}\frac{\partial p}{\partial z}\\&=\frac{\partial p}{\partial\phi}+\vec{x}\cdot\frac{\partial\hat{u}}{\partial\phi}\frac{\partial p}{\partial s}+\left(\vec{x}\cdot\frac{\partial\hat{n}}{\partial\phi}+\tan\theta\vec{x}\cdot\frac{\partial\hat{v}}{\partial\phi}\right)\frac{\partial p}{\partial t}-\sec\theta\vec{x}\cdot\frac{\partial\hat{v}}{\partial\phi}\frac{\partial p}{\partial z}\\&=\frac{\partial p}{\partial\phi}+(\cos\theta\vec{x}\cdot\hat{n}+\sin\theta\vec{x}\cdot\hat{v})\frac{\partial p}{\partial s}-\sec\theta\vec{x}\cdot\hat{u}\frac{\partial p}{\partial t}+\tan\theta\vec{x}\cdot\hat{u}\frac{\partial p}{\partial z}\\&=\frac{\partial p}{\partial\phi}+t\cos\theta\frac{\partial p}{\partial s}-s\sec\theta\frac{\partial p}{\partial t}+s\tan\theta\frac{\partial p}{\partial z}.\end{aligned} \quad \text{(B.4)}$$

Here we used $\partial n/\partial\varphi=-\cos\theta\hat{u}$, $\partial\hat{u}/\partial\varphi=\cos\theta n\hat{}+\sin\theta v\hat{}$ and $\partial v/\partial\varphi=-\sin\theta\hat{u}$. Using (B.3), we can rewrite the second term of (11) with a $-\cos\theta$ factor as

$$\cos\theta\sigma^2(\hat{n}\cdot\nabla)(\hat{u}\cdot\nabla)q(\vec{x},\hat{n})=\cos\theta\sigma^2\frac{\partial^2 p}{\partial s\partial t}. \quad \text{(B.5)}$$

Adding (B.4) and (B.5), we convert the first histo-image consistency equation (11) into the following sinogram consistency equation

$$\frac{\partial p}{\partial \phi}+t\cos\theta\frac{\partial p}{\partial s}-s\sec\theta\frac{\partial p}{\partial t}+s\tan\theta\frac{\partial p}{\partial z}+\sigma^2\cos\theta\frac{\partial^2 p}{\partial s\partial t}=0. \quad \text{(B.6)}$$

Using (14) and (B.1), we can rewrite the first term of (12) with a negative sign as

$$\begin{aligned}
-\hat{v}\cdot\nabla_{\hat{n}}q\left(\overrightarrow{x},\hat{n}\right)&=\tfrac{d}{d\theta}p\left(t,s,\phi,z,\theta\right)\big|_{\overrightarrow{x}}\\
&=\tfrac{\partial p}{\partial\theta}+\tfrac{\partial\left(\overrightarrow{x}\cdot\hat{u}\right)}{\partial\theta}\big|_{\overrightarrow{x}}\tfrac{\partial p}{\partial s}+\tfrac{\partial\left(\overrightarrow{x}\cdot\hat{n}+\tan\theta\overrightarrow{x}\cdot\hat{v}\right)}{\partial\theta}\big|_{\overrightarrow{x}}\tfrac{\partial p}{\partial t}+\tfrac{\partial\left(-\sec\theta\overrightarrow{x}\cdot\hat{v}\right)}{\partial\theta}\big|_{\overrightarrow{x}}\tfrac{\partial p}{\partial z}\\
&=\tfrac{\partial p}{\partial\theta}+\overrightarrow{x}\cdot\tfrac{\partial\hat{u}}{\partial\theta}\tfrac{\partial p}{\partial s}+\left(\overrightarrow{x}\cdot\tfrac{\partial\hat{n}}{\partial\theta}+\tan\theta\overrightarrow{x}\cdot\tfrac{\partial\hat{v}}{\partial\theta}+\tfrac{\partial\tan\theta}{\partial\theta}\overrightarrow{x}\cdot\hat{v}\right)\tfrac{\partial p}{\partial t}-\left(\sec\theta\overrightarrow{x}\cdot\tfrac{\partial\hat{v}}{\partial\theta}+\tfrac{\partial\sec\theta}{\partial\theta}\overrightarrow{x}\cdot\hat{v}\right)\tfrac{\partial p}{\partial z}\\
&=\tfrac{\partial p}{\partial\theta}+(-\overrightarrow{x}\cdot\hat{v}+\tan\theta\overrightarrow{x}\cdot\hat{n}+\sec^2\theta\overrightarrow{x}\cdot\hat{v})\tfrac{\partial p}{\partial t}-(\sec\theta\overrightarrow{x}\cdot\hat{n}+\sec\theta\tan\theta\overrightarrow{x}\cdot\hat{v})\tfrac{\partial p}{\partial z}\\
&=\tfrac{\partial p}{\partial\theta}+\tan\theta\left(\overrightarrow{x}\cdot\hat{n}+\tan\theta\overrightarrow{x}\cdot\hat{v}\right)\tfrac{\partial p}{\partial t}-\sec\theta\left(\overrightarrow{x}\cdot\hat{n}+\tan\theta\overrightarrow{x}\cdot\hat{v}\right)\tfrac{\partial p}{\partial z}\\
&=\tfrac{\partial p}{\partial\theta}+t\tan\theta\tfrac{\partial p}{\partial t}-t\sec\theta\tfrac{\partial p}{\partial z}.
\end{aligned} \quad \text{(B.7)}$$

Here we used $\partial n/\partial\theta=-v$, $\partial\hat{u}/\partial\theta=0$ and $\partial v/\partial\theta=n$. Using (B.3), we can rewrite the second term of (12) with a negative sign as

$$\sigma^2\left(\hat{n}\cdot\nabla\right)\left(\hat{v}\cdot\nabla\right)q(\overrightarrow{x},\hat{n})=\sigma^2\tan\theta\frac{\partial^2 p}{\partial^2 t}-\sigma^2\sec\theta\frac{\partial^2 p}{\partial z\partial t}. \quad \text{(B.8)}$$

Adding (B.7) and (B.8), we convert the second histo-image consistency equation (12) into the following sinogram consistency equation

$$\frac{\partial p}{\partial\theta}+t\tan\theta\frac{\partial p}{\partial t}-t\sec\theta\frac{\partial p}{\partial z}+\sigma^2\tan\theta\frac{\partial^2 p}{\partial t^2}-\sigma^2\sec\theta\frac{\partial^2 p}{\partial z\partial t}=0. \quad \text{(B.9)}$$

Equations (B.6) and (B.9) are identical to equations (4) and (2) with $\tan\theta=\delta$ in (Defrise et al. 2013). After removing the partial derivative with respect to z and using $\theta=0$, (B.6) becomes equation (8) in (Defrise et al. 2012), which was used to determine the attenuation sinogram from 2D TOF-PET data. Similar to (B.6) and (B.9), we can convert (15) to

$$\sec\theta\frac{\partial^2 p}{\partial z\partial\phi}-\tan\theta\frac{\partial^2 p}{\partial\phi\partial t}-s\left(\sec^2\theta+\tan^2\theta\right)\frac{\partial^2 p}{\partial z\partial t}+s\tan\theta\sec\theta\frac{\partial^2 p}{\partial z^2}+s\tan\theta\sec\theta\frac{\partial^2 p}{\partial t^2}-\tan\theta\cos\theta\frac{\partial p}{\partial s}+\cos\theta\frac{\partial^2 p}{\partial s\partial\theta}=0. \quad \text{(B.10)}$$

Equation (B.10) is just $v\cdot\nabla(11)-\hat{u}\cdot\nabla(12)$, and it is equivalent to equation (6) in (Defrise et al. 2008) and equation (3) in (Defrise et al. 2013). After removing the three terms with the partial derivative of t, (B.10) becomes John's equation for non-TOF PET data (John 1938, John 1982, Defrise and Liu 1999, Defrise et al. 2013).

Appendix C. Spatially invariant attenuation gradients along TOF direction

The attenuation histo-image $a(x,\vec{n})$ is invariant along the TOF direction n. To verify the internal consistency of the derivations in Section 2.4, we check below that the LS solution, (31) and (32), also has spatially invariant property along the TOF direction. Recalling that the argument of m and its derivatives in (30) is $(x_0+ln,\hat{n})$, we can change the integration variable $l+l_0\rightarrow l$ and rewrite the quantities in (30) at x_0+l_0n for some l_0 as

$$\begin{aligned} H_{11}(\vec{x}_0+l_0\hat{n},\hat{n}) &= H_{11}(\vec{x}_0,\hat{n})+l_0^2H_{22}(\vec{x}_0,\hat{n})-2l_0H_{12}(\vec{x}_0,\hat{n}),\\ H_{12}(\vec{x}_0+l_0\hat{n},\hat{n}) &= H_{12}(\vec{x}_0,\hat{n})-l_0H_{22}(\vec{x}_0,\hat{n}),\\ H_{22}(\vec{x}_0+l_0\hat{n},\hat{n}) &= H_{22}(\vec{x}_0,\hat{n}),\\ J_1(\vec{x}_0+l_0\hat{n},\hat{n}) &= J_1(\vec{x}_0,\hat{n})-l_0J_2(\vec{x}_0,\hat{n}),\\ J_2(\vec{x}_0+l_0\hat{n},n) &= J_2(\vec{x}_0,\hat{n}). \end{aligned} \quad \text{(C.1)}$$

Then (29) at $\vec{x_0}+l_0\hat{n}$ becomes

$$\begin{bmatrix} H_{11}+l_0^2H_{22}-2l_0H_{12} & H_{12}-l_0H_{22} \\ H_{12}-l_0H_{22} & H_{22} \end{bmatrix} \begin{bmatrix} -(\hat{u}\cdot\nabla)\log a(\vec{x}_0+l_0\hat{n},\hat{n}) \\ (\hat{u}\cdot\nabla_{\hat{n}})\log a(\vec{x}_0+l_0\hat{n},\hat{n}) \end{bmatrix} = \begin{bmatrix} J_1-l_0J_2 \\ J_2 \end{bmatrix}. \quad \text{(C.2)}$$

Subtracting $-l_0$ times the second row from the first row, we obtain

$$\begin{bmatrix} H_{11} & H_{12} \\ H_{12} & H_{22} \end{bmatrix} \begin{bmatrix} 1 & 0 \\ -l_0 & 1 \end{bmatrix} \begin{bmatrix} -(\hat{u}\cdot\nabla)\log a(\vec{x}_0+l_0\hat{n},\hat{n}) \\ (\hat{u}\cdot\nabla_{\hat{n}})\log a(\vec{x}_0+l_0\hat{n},\hat{n}) \end{bmatrix} = \begin{bmatrix} J_1 \\ J_2 \end{bmatrix}. \quad \text{(C.3)}$$

From (C.3), we obtain the following solution

$$-\hat{u}\cdot\nabla\log a(\vec{x}_0+l_0\hat{n},\hat{n}) = \frac{H_{22}J_1-H_{12}J_2}{H_{11}H_{22}-H_{12}^2}. \quad \text{(C.4)}$$

$$\hat{u}\cdot\nabla_{\hat{n}}\log a(\vec{x}_0+l_0\hat{n},\hat{n})+l_0\hat{u}\cdot\nabla\log a(\vec{x}_0+l_0\hat{n},\hat{n}) = \frac{H_{11}J_2-H_{12}J_1}{H_{11}H_{22}-H_{12}^2}. \quad \text{(C.5)}$$

After comparing (31, 32) and (C.4, C.5), we return to (22) and (24).

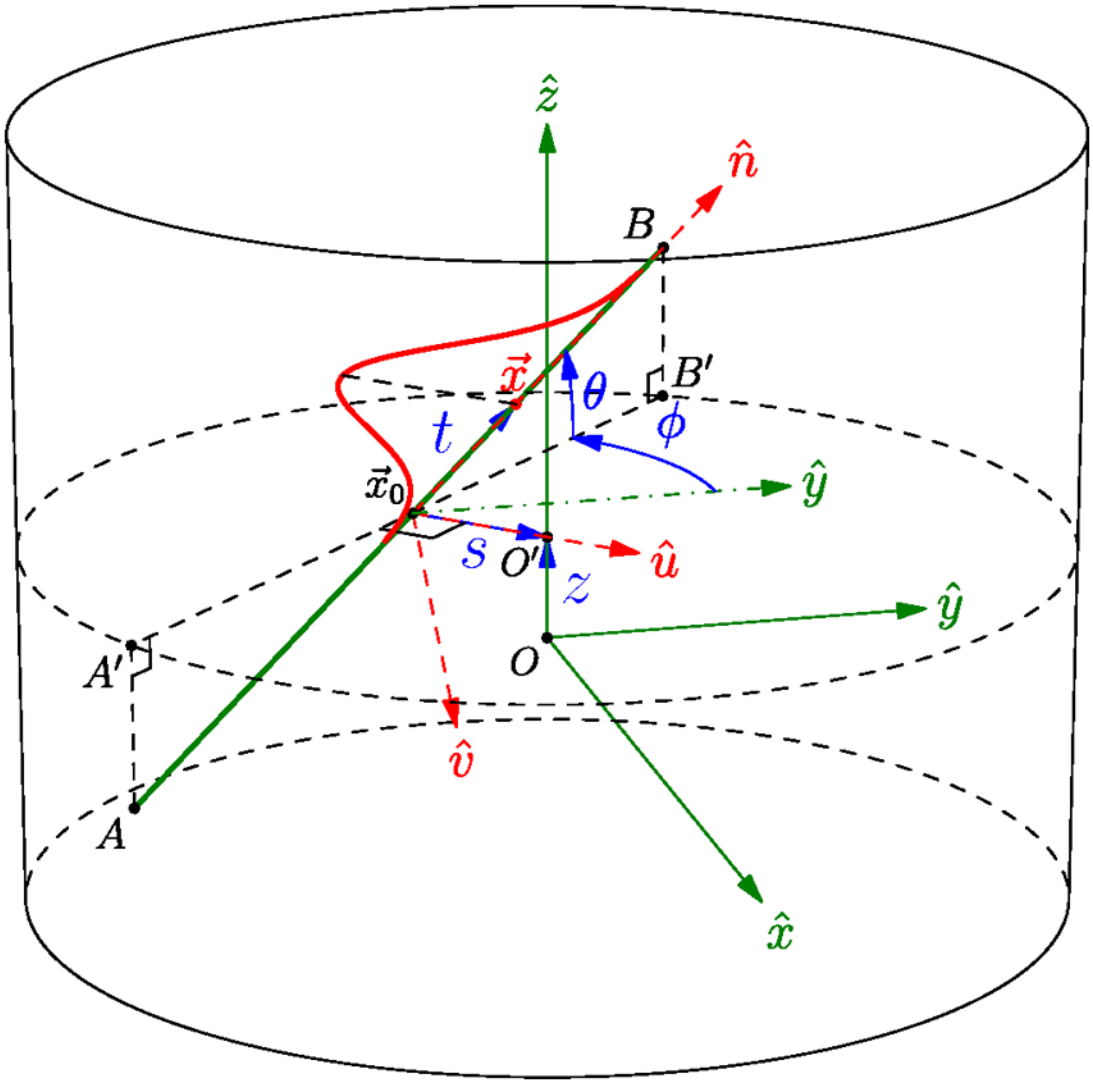

Figure 1.

Data parameterization of histo-image for a multi-ring TOF-PET scanner. *A* coincidence event between detectors *A* and *B* with TOF difference *t* can be parameterized in histo-image format by the most likely position x along $\vec{n}$ and the TOF direction n, the TOF profile is centered at position x along n, and x_0 is the midpoint between *A* and *B*. The event can also be parameterized in the sinogram format by the variables t, s, z, φ and θ.

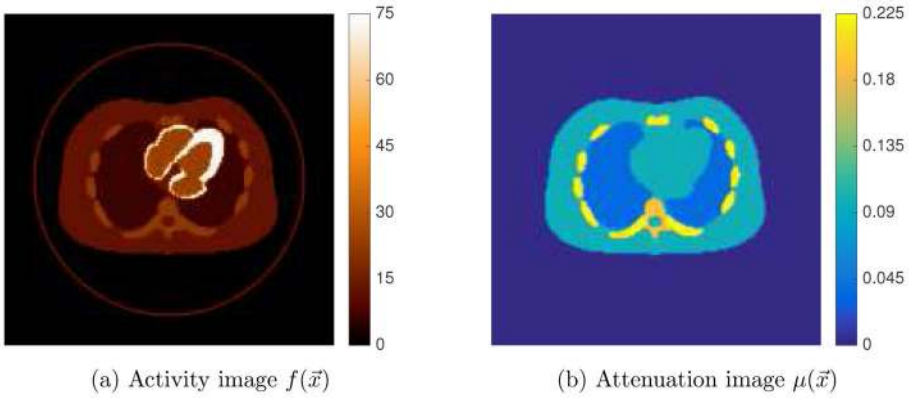

(a) Activity image $f(\vec{x})$ (b) Attenuation image $\mu(\vec{x})$

Figure 2.

Activity and attenuation images of the simulated XCAT phantom. The image size is 70.4 cm × 70.4 cm, and the simulated TOF resolution was 7.5 cm FWHM, corresponding to time resolution of about 500 ps.

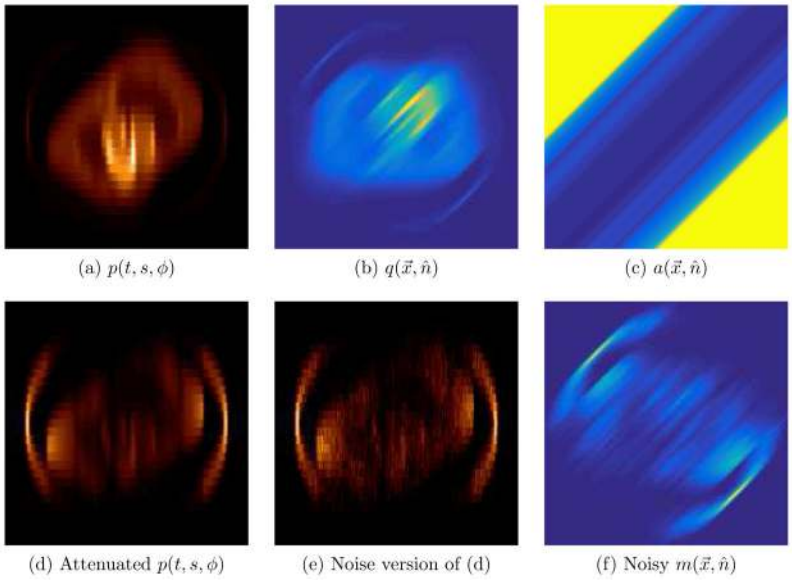

Figure 3.

Histo-image generation along direction n ât φ=135°. (a) is a TOF sinogram $p(t, s, \varphi)$ at the fixed direction, (b) is the CW activity histo-image obtained from (a), (c) is an attenuation factors in histo-image format, (d) is the attenuated TOF sinogram, (e) is obtained from (d) by adding Poisson noise, (f) is the CW histo-image obtained from (e). For TOF sinograms in (a), (d) and (e), the horizontal and vertical axes represent radial variable s and TOF variable t, respectively. For the histo-images in (b), (c,) and (f), the axes are the cartesian coordinates in image space. Note that for this 2D example the axes in the sinograms are rotated by φ compared with the histo-images.

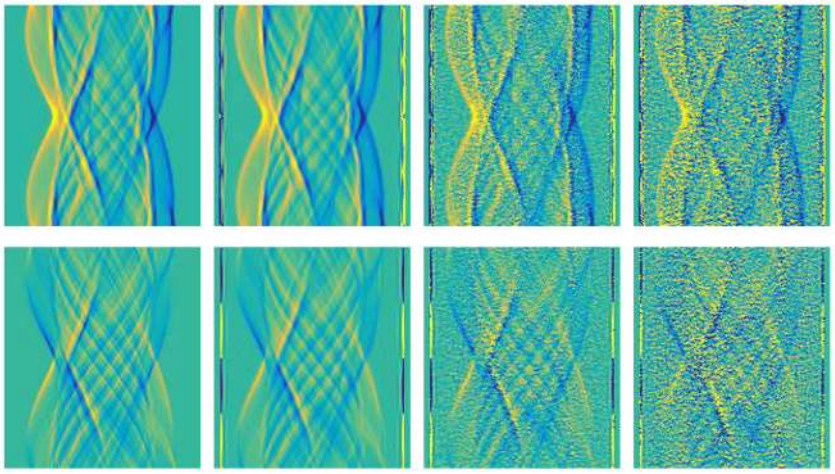

Figure 4.

Estimation of directional derivatives $-\hat{u} \cdot \nabla \log \boldsymbol{a}$ (first row) and $\hat{u} \cdot \nabla_n \log \boldsymbol{a}$ (second row), in sinogram format. The approximation of the true derivatives using central difference is also shown in the first column for comparison. The second to the fourth columns are the estimated derivatives from the CW histo-images of noise-free, moderate-noise and high-noise cases, respectively.

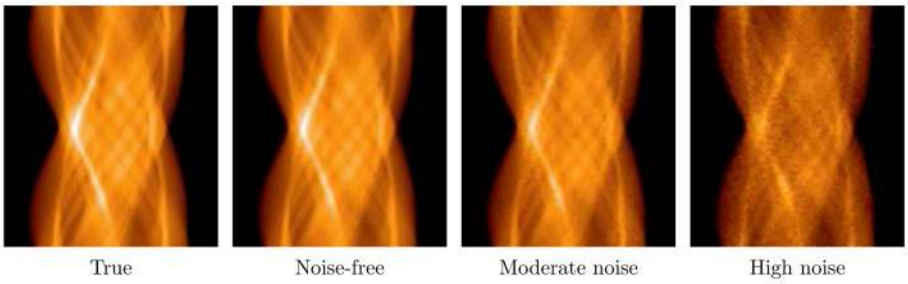

Figure 5.
The true and estimated attenuation in sinogram format for the noise-free, moderate and high noise cases.

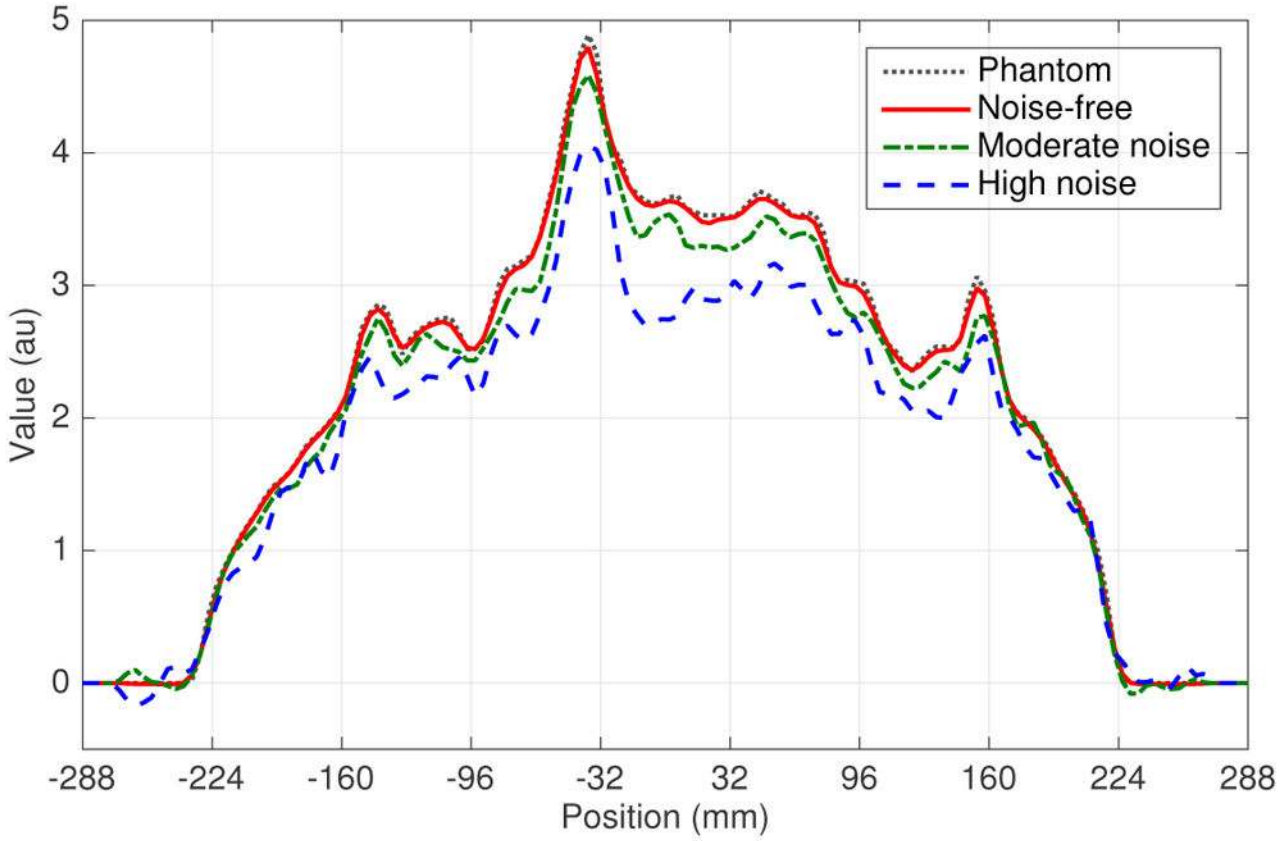

Figure 6.

Horizontal profiles through the sinogram shown in figure 5 at $\varphi = 135°$. The dotted curve denotes the true profile; the solid, dash-dotted and dashed curves denote the profiles through the noise-free and two noisy estimated sinograms.

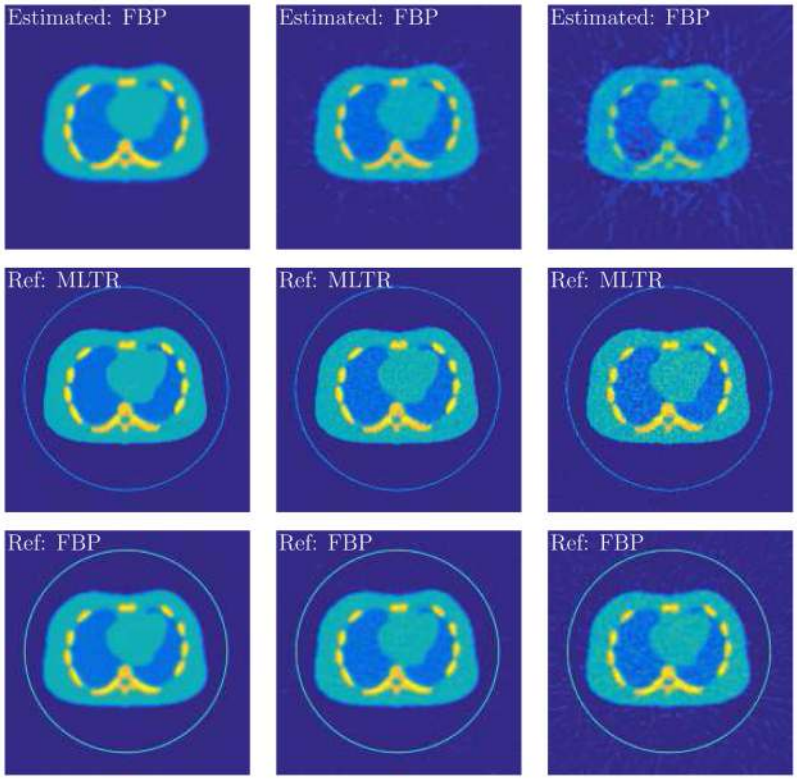

Figure 7.

Reconstructed attenuation images from simulated data without noise (left column), with moderate noise (middle column) and with high noise (right column). The attenuation images estimated using the LS solution (31,32) and fast solver (43) are shown in the first row. The reference images reconstructed using MLTR and FBP are shown in the second and third rows, respectively. The reference images were reconstructed from the TOF-integrated attenuated emission histo-image with the assumption that the true activity distribution was known.

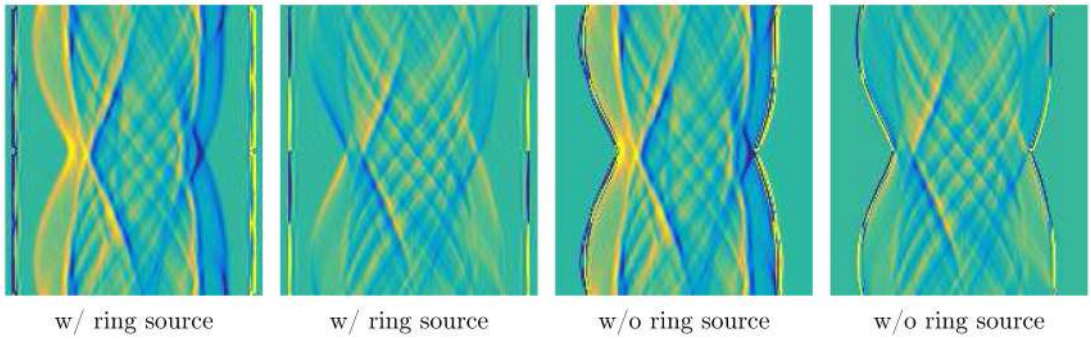

Figure 8.

Comparison of the directional derivatives estimated from the noise-free data with and without ring source. The derivatives $-\hat{u} \cdot \nabla \log \boldsymbol{a}$ and $\hat{u} \cdot \nabla_n \log \boldsymbol{a}$ in the first and second columns are the same images as in the second column of figure 4.